NANO LETTERS

pubs.acs.org/NanoLett Letter

Photonic Spin-Multiplexing Metasurface for Switchable Spiral Phase Contrast Imaging

Pengcheng Huo, Cheng Zhang, Wenqi Zhu, Mingze Liu, Song Zhang, Si Zhang, Lu Chen, Henri J. Lezec, Amit Agrawal, Yanqing Lu, and Ting Xu*

Cite This: *Nano Lett.* 2020, 20, 2791−2798 Read Online

ACCESS | Metrics & More | Article Recommendations | Supporting Information

ABSTRACT: As the two most representative operation modes in an optical imaging system, bright-field imaging and phase contrast imaging can extract different morphological information on an object. Developing a miniature and low-cost system capable of switching between these two imaging modes is thus very attractive for a number of applications, such as biomedical imaging. Here, we propose and demonstrate that a Fourier transform setup incorporating an all-dielectric metasurface can perform a two-dimensional spatial differentiation operation and thus achieve isotropic edge detection. In addition, the metasurface can provide two spin-dependent, uncorrelated phase profiles across the entire visible spectrum. Therefore, based on the spin-state of incident light, the system can be used for either diffraction-limited bright-field imaging or isotropic edge-enhanced phase contrast imaging. Combined with the advantages of planar architecture and ultrathin thickness of the metasurface, we envision this approach may open new vistas in the very interdisciplinary field of imaging and microscopy.

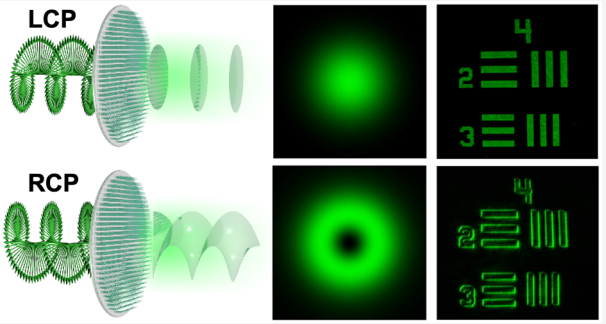

KEYWORDS: *Metasurface, phase contrast imaging, edge detection, orbital angular momentum*

Downloaded via NANJING UNIV on May 15, 2025 at 08:40:04 (UTC).
See https://pubs.acs.org/sharingguidelines for options on how to legitimately share published articles.

Fast and reliable detection and recognition of an object is one of the fundamental capabilities required in applications such as imaging, microscopy, machine learning, and artificial intelligence. Although convectional bright-field imaging method can provide overall morphologies of amplitude objects, increasing image contrast, and precisely distinguishing the edges of phase objects, such as certain biological samples that typically lack substantial amounts of natural pigments,[1] is especially important. To enhance the optical imaging process, spatial filtering to modulate the input light field by placing an appropriate optical element in the incident beam path and changing its phase, amplitude, and spatial frequency at the sample plane has been proposed.[2] On the basis of this operation, many phase contrast methods have been demonstrated, such as Zernike phase contrast imaging[3] and differential interference contrast imaging.[4] Recently, structured light to perform spatial differentiation for analog optical computing has shown the potentials for the application in image processing of edge detection.[5−11] However, most of the demonstrations on spatial differentiation are one-dimensional, which typically leads to anisotropic edge detection of the object and thus is not perfectly suited to imaging applications.

With further studies on radial Hilbert transform filtering,[12] it has been suggested that the opposite halves of any radial line of the spiral phase element will introduce a phase difference of π between the positive and negative spatial frequencies of incident light field, which leads to a strong isotropic edge contrast enhancement of observed amplitude and phase objects.[13−16] Since it only extracts important information and records basic geometric features related to the edges of an object, the spiral phase contrast imaging greatly reduces the amount of data to be processed. To date, the primary realization of spiral phase contrast imaging is accomplished using a liquid crystal-based spatial light modulator, which offers dynamic control over the optical amplitude and phase at the expense of large volume, limited resolution, and high cost.[17−19] Therefore, how to develop a miniature, high-resolution, low-cost, and controllable spiral phase contrast imaging system for both amplitude and phase objects is very attractive for many practical applications.

In recent years, metasurfaces, ultrathin optical elements consisting of an array of subwavelength nanostructures, have attracted a lot of attention and made significant progress toward both the temporal and spatial domain manipulation of

Received: February 3, 2020
Revised: February 27, 2020
Published: March 10, 2020

ACS Publications © 2020 American Chemical Society

https://dx.doi.org/10.1021/acs.nanolett.0c00471
Nano Lett. 2020, 20, 2791−2798

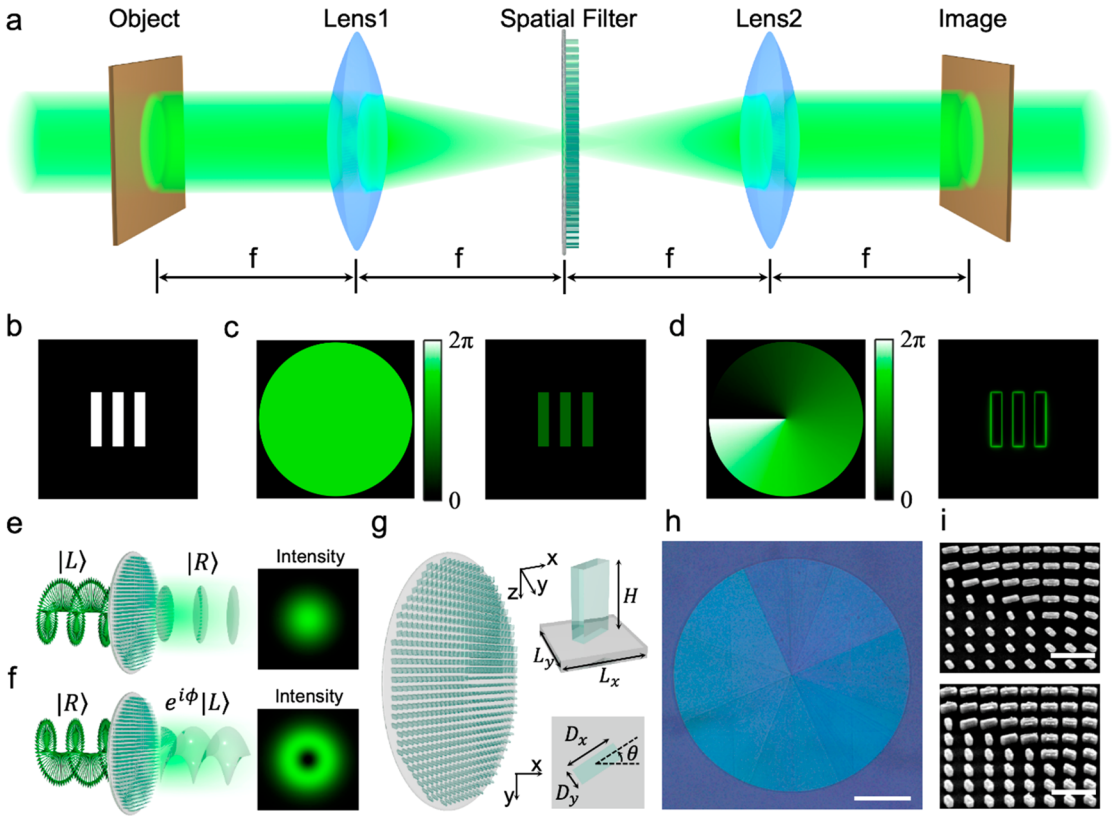

Figure 1. (a) Schematic of the Fourier transform setup for spatial filtering. An object (b) illuminated with a plane wave will diffract the light to outer regions in the Fourier plane, where the metasurface is placed. With a constant phase (c) or an ideal spiral phase (d) implemented in the metasurface, the calculated results of the image plane show a traditional bright image and an edge enhanced image. (e,f) Schematic of the concept for spin-dependent function control. (e) For light incident on the device with LCP, the metasurface imprints a masking function (M_1) on the output beam resulting in a constant phase profile and a Gaussian intensity distribution and flips the handedness of the incident polarization. (f) For light incident on the same device with RCP, the metasurface imprints another masking function (M_2), resulting in a spiral phase profile and a donut-shaped intensity distribution, and again flips the handedness of the polarization. (g) Schematic of the designed all-dielectric metasurface spatial filter to implement the function in (e,f). Inset: perspective and top view of the metasurface unit-cell formed by amorphous TiO_2 nanopillar sitting on a silica substrate. (h) Optical photograph of the fabricated metasurface device. Scale bar: 500 μm. (i) Top view and oblique view of the SEM images of TiO_2 nanopillar array. Scale bar: 1 μm.

optical wavefronts.[20−26] These efforts push the engineering optics into a new era: Engineering Optics 2.0.[27,28] Arbitrary control over the amplitude, phase, and polarization of light has been verified in various embodiments of nanophotonic devices such as metalenses,[29,30] metaholograms,[31,32] spin-to-orbital angular momentum conversion,[33−39] imaging-based biosensor,[40] nonlinear optics,[41,42] and multispectral chiral imaging.[43] Here, by designing and embedding a photonic spin-multiplexing dielectric metasurface in the focal plane of a Fourier transform setup, we demonstrate that the system is capable of dynamically switching between the bright-field imaging mode and spiral phase contrast imaging mode only by changing the spin-state of incident light. The spiral phase filtering operation of the metasurface further enables two-dimensional spatial differentiation to the incident light field. As a result, it can be used for isotropic edge-enhanced detection of undyed biological samples. Combined with the advantages of planar architecture and ultrathin thickness offered by dielectric metasurface, this generalized method will expand its impact and open new possibilities of creating compact and low-cost multifunctional microscopes for biomedical imaging and surface defect detection.

In a Fourier transform setup (Figure 1a), the electric field distribution of an incident plane wave illuminating an object can be written as $E_{in}(x, y)$. A spatial filter designed to physically implement a complex masking function $M(\rho, \phi)$ is placed at the Fourier plane of the lens 1. After passing through the filter and undergoing phase shift and amplitude transformation, the light field is reshaped by the lens 2, yielding an output electric field distribution $E_{out}(x, y)$ at the image plane. The output and input fields can be associated according to the following relation

$$E_{out}(x, y) = E_{in}(x, y) \otimes m(r, \varphi) \quad (1)$$

Here, (x, y) is the spatial coordinates at the object (image) plane and (r, φ) is the corresponding polar coordinates. The symbol $\otimes$ represents convolution and $m(r, \varphi) = F\{M(\rho, \phi)\}$ denotes the Fourier transform of the masking function, which acts as the point-spread function (PSF). (ρ, ϕ) represents the polar coordinates in the Fourier plane and is related to Cartesian coordinates (u, v) in the Fourier plane as $\rho = \sqrt{u^2 + v^2}$ and $\phi = \tan^{-1}(v/u)$. Therefore, in principle, desirable light fields at the image plane can be achieved by modulating the masking function $M(\rho, \phi)$ of the spatial filter at the Fourier plane.

For example, for an object containing three rectangular slots illuminated by a plane wave, as shown in Figure 1b, a masking function including a constant phase and amplitude $M_1(\rho, \phi) =$

https://dx.doi.org/10.1021/acs.nanolett.0c00471
Nano Lett. 2020, 20, 2791−2798

$\exp(ic_0)$, where c_0 is a constant, will generate a bright-field image at the image plane (Figure 1c), like a conventional 4f imaging system. In contrast to the bright-field image, if the masking function becomes a spiral phase plate $M_2(\rho, \phi) = \exp(i\phi)$, the corresponding PSF $m_2(r, \varphi)$ can be regarded as the formation of a vortex that has a donut-shaped intensity distribution and a spiral phase profile changing from 0 to 2π for one turn (SI Note 1 for details). In the convolution process of eq 1, m_2 with a vortex element will be weighted to superimpose on each point of the input light field E_{in} and then integrated over the whole area to determine the amplitude of the corresponding point of the output light field E_{out}. Because of the phase difference of π along the opposite azimuth of the vortex element, integrating the uniform area of E_{in} will lead to destructive interference and a dark background. In contrast, arbitrarily unevenness including amplitude gradient and phase gradient in the region of integration will remove this destructive interference and result in bright regions. In Figure 1d, the calculated result of the image plane shows an isotropic effect of spiral phase contrast imaging, which is not sensitive to the absolute phase and amplitude of the object but to the phase and amplitude gradients. In addition, the calculated spatial spectral transfer function is shown in SI Figure S1. Combined with the analytical result of SI eq S7, it shows that spiral phase filtering operation is equivalent to two-dimensional spatial differentiation of the incident light field.

In synergy with the polarization states of incident light, ultrathin planar metasurface provides an effective approach to impart photonic spin-multiplexing phases at the Fourier plane. As a result, bright-field imaging and spiral phase contrast imaging can be dynamically switched by the chirality of light using metasurface spatial filter with spin-dependent masking functions. Assume that the incident light upon the metasurface is in two orthogonal spin states $|L\rangle = \frac{1}{\sqrt{2}}\begin{bmatrix}1\\ i\end{bmatrix}$ and $|R\rangle = \frac{1}{\sqrt{2}}\begin{bmatrix}1\\ -i\end{bmatrix}$, where $|L\rangle$ and $|R\rangle$ denote left- and right-circular polarization (LCP and RCP) in the linear polarization basis. Figure 1e,f shows schematic of the concept for spin-multiplexing function control. In order to independently implement two uncorrelated masking functions (M_1 and M_2) for the incident plane wave propagating along the z-direction in LCP and RCP states, respectively, the metasurface should simultaneously perform the beam transformation

$$\text{LCP: } |L\rangle \rightarrow M_1|R\rangle \tag{2}$$

$$\text{RCP: } |R\rangle \rightarrow M_2|L\rangle \tag{3}$$

For LCP incident light, the metasurface spatial filter imprints a masking function (M_1) on the output beam with a constant phase profile and a Gaussian intensity distribution and flips the handedness of the incident polarization to RCP (Figure 1e). On the other hand, for RCP incident light the metasurface imprints another masking function (M_2) with a spiral phase profile and a donut-shaped intensity distribution and again flips the handedness of the polarization to LCP (Figure 1f). Consequently, the metasurface spatial filter can be expressed by a Jones matrix J which acts independently on the two orthogonal input states of light and takes the form

$$J = \frac{1}{2}\begin{bmatrix} (M_1 + M_2) & -i(M_1 - M_2) \\ -i(M_1 - M_2) & -(M_1 + M_2) \end{bmatrix} \tag{4}$$

The unitary of this matrix guarantees that it can be diagonalized by solving the characteristic equation. The eigenvalues and eigenvectors of this Jones matrix require that the elements of the metasurface spatial filter have a birefringent response with the phase shifts (φ_x, φ_y) along the two perpendicular symmetry axes and the orientation angle θ of fast axes as a function of the reference coordinate. We can find the analytical expression for required phase shifts and orientation angles as follows (SI Note 2 for details)

$$\varphi_x = \frac{1}{2}(c_0 + \phi) \tag{5}$$

$$\varphi_y = \frac{1}{2}(c_0 + \phi) - \pi \tag{6}$$

$$\theta = \frac{1}{4}(c_0 - \phi) \tag{7}$$

Therefore, it is imperative to find a set of nanostructures with proper phase shifts and orientation angles covering the full phase range $[0, 2\pi]$.

Figure 1g shows the schematic diagram of the proposed metasurface filter, which contains titanium dioxide (TiO_2) nanopillars arranged periodically in a square lattice with a constant $L_x = L_y = 450$ nm. We choose TiO_2 as the constituent material because of its large index of refraction and low loss at visible frequencies (SI Figure S3). Each of these nanopillars has equal height ($H = 600$ nm) and acts as an individual nanoscale half-wave plate (HWP). The propagation phase shifts φ_x and φ_y along the two symmetry axes are dependent on the in-plane dimensions D_x and D_y, and the geometric phase is controlled by the in-plane rotation angle θ of the fast axis of the nanopillar. On the basis of a suitable combination of propagation phase and geometric phase of the metasurface, two sets of uncorrelated phase profiles can be imparted on the incident light in its respective LCP and RCP states.

A broad range of TiO_2 rectangular nanopillars with a fixed height but varying in-plane dimensions are simulated to find the appropriate structural parameters for designing high efficiency HWP. Each point in the plot of transmission coefficients and phase shifts corresponds to a nanopillar with specific (D_x, D_y) combination for a particular wavelength (SI Figure S4). The degree of discretization of HWP in the full range $[0, 2\pi]$ can be determined by calculating the mean square error function (MSE), which is used to evaluate the effect of segment number (s) in spiral phase on imaging quality as

$$MSE(s) = \frac{\sum_{a=1}^{A}\sum_{b=1}^{B}|I(a, b) - I_s(a, b)|^2}{A \times B} \tag{8}$$

where $I(a, b)$ and $I_s(a, b)$ represent the imaging results by adopting an ideal and the s-segment spiral phase filter, respectively. A and B are the pixel sampling number of the generated image along the x- and y-directions, respectively. Considering the trade-off between imaging quality and design complexity, the optimization operation yields $s = 16$ (SI Note 3 for details). The structural parameters of a set of 16 nanopillars are optimized so that all the HWPs' transmission coefficients and polarization conversion efficiencies are sufficiently high across the entire visible region (SI Figure S9), which would benefit the imaging efficiency from the metasurface spatial filter. In addition, as shown in SI Figure S10, the normalized energy density is mainly confined inside the TiO_2 nanopillar.

https://dx.doi.org/10.1021/acs.nanolett.0c00471
Nano Lett. 2020, 20, 2791−2798

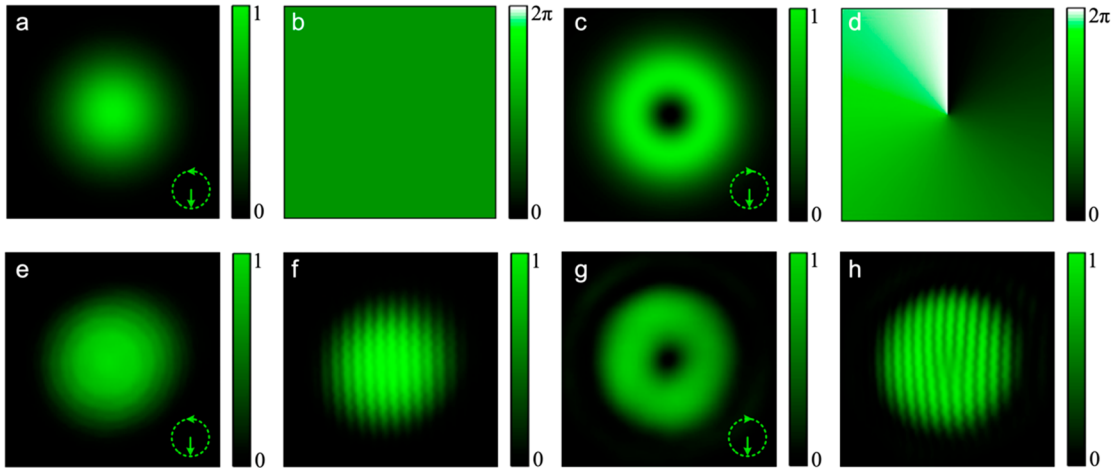

Figure 2. Simulated and experimental demonstration of the two independent masking functions imposed on the spin-dependent metasurface spatial filter. Top panels: simulated output states of the metasurface spatial filter at the wavelength of 530 nm. An intensity distribution (a) and a phase profile (b) shows a Gaussian beam for LCP incident light, the donut intensity distribution (c) and the spiral phase profile (d) shows a $1\hbar$ OAM beam for RCP incident light. Lower panels show measured intensity distributions (e) and (g) and nonparaxial interference patterns with a plane wavefront (f) and (h) of output states corresponding to LCP and RCP incident light at the wavelength of 530 nm, respectively. Insets show the handedness of incident light.

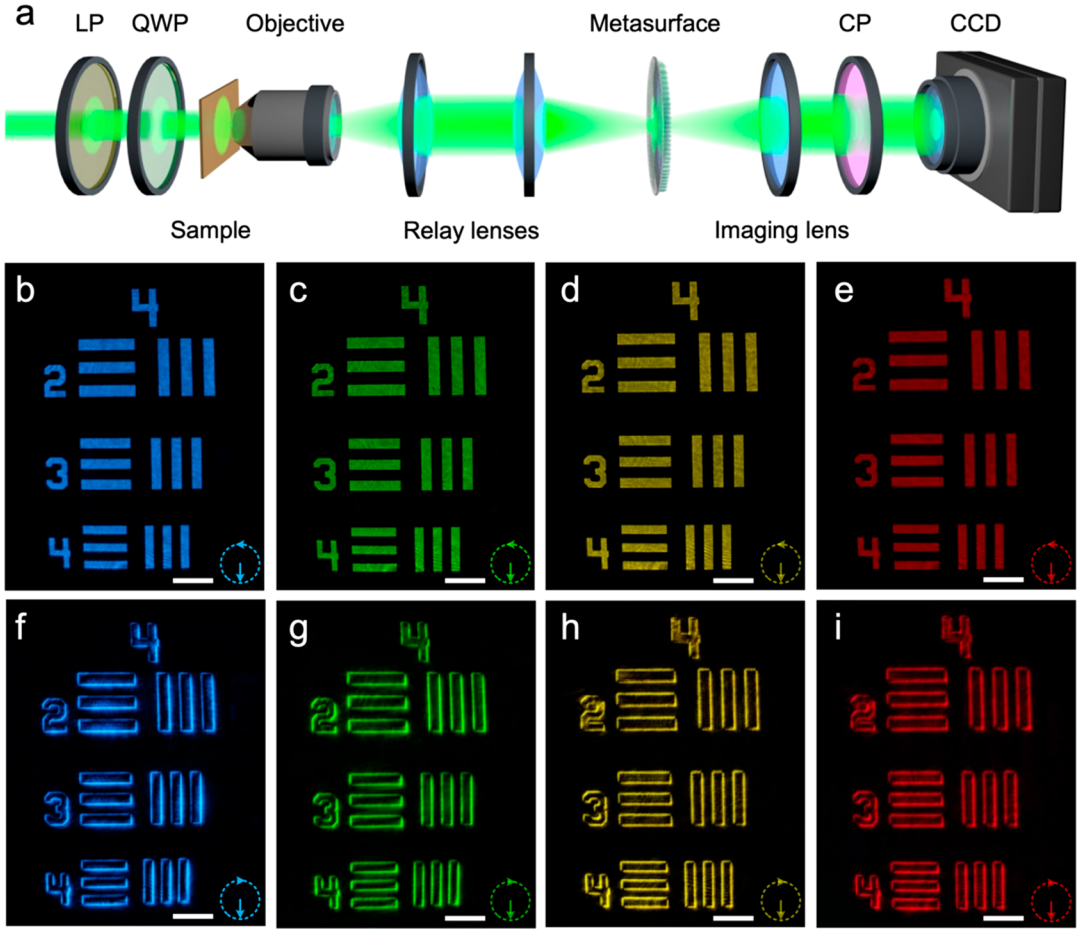

Figure 3. (a) Sketch of the experimental setup for spin-dependent spiral phase contrast imaging. LP and QWP can make the incident light with circular polarization. CP can be used to eliminate background light in the optical path. (b–e) The bright-field image of the resolution test chart under the LCP incident light at the wavelength of 480, 530, 580, and 630 nm, respectively. (f–i) Spiral phase contrast images of the resolution test chart under the RCP incident light at the same wavelengths. Insets show the handedness of incident light. Scale bars: 100 μm.

The coupling effect between neighboring nanopillars is very weak, and thus each nanopillar can be regarded as an isolated rectangular waveguide. This allows the phase design for each nanopillar element to still be accurate when they are arranged in a square lattice to form the metasurface spatial filter. Figure 1h,i exhibits the optical photograph of the fabricated TiO_2

https://dx.doi.org/10.1021/acs.nanolett.0c00471
Nano Lett. 2020, 20, 2791−2798

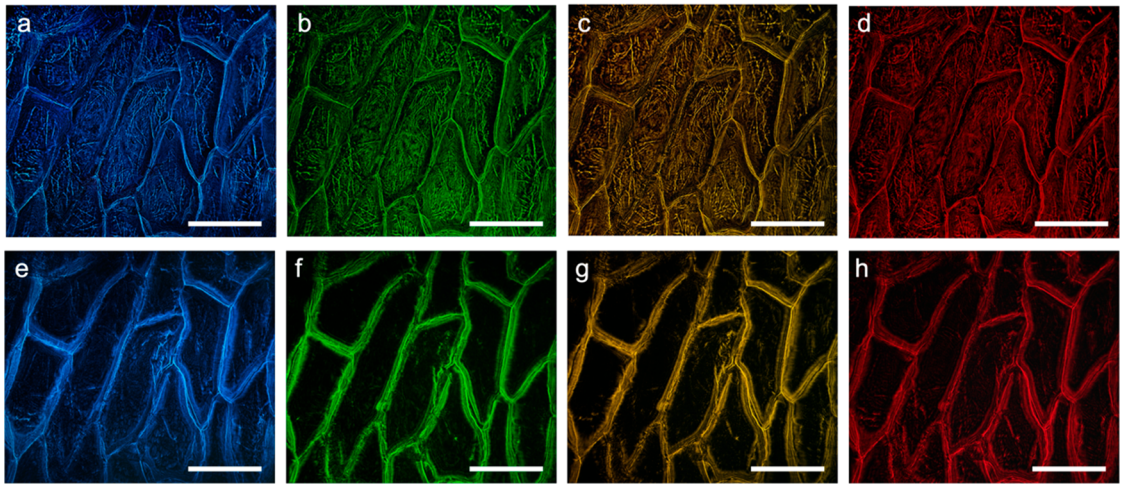

Figure 4. Images of the undyed onion epidermal cells with a 20× objective lens. (a−d) Traditional bright-field images captured with LCP incident light at the wavelength of 480, 530, 580, and 630 nm, respectively. (e−h) Spiral phase contrast images captured with RCP incident light at the corresponding wavelengths. Scale bar: 100 μm.

metasurface spatial filter of 2 mm diameter and the scanning electron microscope (SEM) images of the TiO_2 nanopillar array, respectively. The detailed fabrication process is described in Methods.

To fully characterize the two independent masking functions imposed on the spin-dependent metasurface spatial filter, the far-field intensity distributions and phase profiles of the output states have been numerically simulated and experimentally measured upon illumination with a circularly polarized Gaussian beam. At a free-space wavelength of 530 nm, the Gaussian intensity distribution (Figure 2a) and a constant phase profile (Figure 2b) demonstrate that the input Gaussian beam with LCP can pass through the metasurface spatial filter without any change except for flipping the handedness of the incident polarization. Once switching the incident light from LCP to RCP, the far-field output state shows a donut-shaped intensity distribution (Figure 2c) and a spiral phase profile (Figure 2d), indicating that the transmitted beam carries 1$\hbar$ orbital angular momentum (OAM) while reversing the handedness. As shown in Figure 2e,g, the experimentally measured intensity distributions for LCP and RCP incident light at a wavelength of 530 nm are consistent with the simulated ones. To clarify the phase profiles, nonparaxial interference measurements have been carried out and the relevant results are shown in Figure 2f for LCP light and Figure 2h for RCP light. The interference patterns of equidistant stripes and forklike stripes respectively demonstrate that the metasurface spatial filter endowed with the masking function M_1 and M_2 can independently shape the input chiral light to the desired states. Furthermore, the ability of spin-multiplexing metasurface spatial filter to shape incident light also has been experimentally demonstrated at other wavelengths of the visible region (SI Figure S11). The measured shaping efficiency of the metasurface spatial filter in the visible range can reach up to 50% (SI Figure S12). This is mainly due to the low-loss material selection of TiO_2 and geometrical parameter optimization of HWPs, that are both helpful in improving the spatial filtering efficiency of the system.

The experimental setup for switchable spin-dependent bright-field and spiral phase contrast imaging is sketched in Figure 3a. The sample is placed at the object plane and illuminated by a supercontinuum laser attached to an acousto-optic tunable filter (AOTF) system. A linear polarizer (LP) and a quarter-wave plate (QWP) are used to fully change the incident laser beam from linear polarization to circular polarization. A 20× microscope objective is used for image magnification. The rear focal plane of the objective is extended by using a relay system consisting of two lenses, and the metasurface spatial filter is placed at the Fourier plane. Between an imaging lens and a charge coupled device (CCD), a cross circularly polarizer (CP) is used to eliminate the background light that has the same handedness as the input beam.

To demonstrate the functionalities of the imaging system, a 1951 United State Air Force (USAF) resolution test chart is used as an imaging target and illuminated by the wavelength filtered supercontinuum laser. For the LCP incident beam at wavelengths of 480, 530, 580, and 630 nm, Figure 3b−e respectively displays the bright-field images of fourth-parts of the resolution test chart, which are recorded with a 20× magnification objective in transmission mode. These results correspond to the implementation of the constant phase masking function M_1 on the metasurface spatial filter. As the input polarization is switched from LCP to RCP, Figure 3f−i shows the edge-enhanced images of the same target, achieved by implementing the spiral phase masking function M_2 on the metasurface spatial filter. Obviously, the contrast of all pattern edges is enhanced, irrespective of their orientations, which indicates that the spiral phase contrast imaging is isotropic. In addition, the total light intensities between the bright-field image and phase contrast image are almost identical, revealing that the light energy is redistributed without loss in the phase contrast imaging operation. For the two typical imaging modes, the smallest line pair (lp) that can be resolved in the resolution test chart is elements 6 of group 7 (228 lp/mm) and elements 3 of group 7 (161 lp/mm), which corresponds a system resolution of 2.19 and 3.11 μm along all directions (SI Figure S13). In principle, the imaging resolution of the system can be improved by changing the objective lens and increasing the size of the metasurface spatial filter.

One major advantage of phase contrast imaging is that it can readily detect samples with small refractive index difference from the background environment such as biological cells. Therefore, we further carry out the demonstration of

https://dx.doi.org/10.1021/acs.nanolett.0c00471
Nano Lett. 2020, 20, 2791−2798

switchable imaging of unstained onion epidermal cells with a 20× objective lens. Figure 4a–d shows the bright-field images of onion epidermal cells captured with illumination of LCP light at wavelengths of 480, 530, 580, and 630 nm, respectively. Although one can see some organelles inside the cells, small amplitude and phase differences between cell walls and cytoplasm make the single cell boundary indistinguishable. However, the image contrast is completely changed in spiral phase contrast imaging upon illumination with RCP incident light (Figure 4e–h). As expected, the edge-enhanced images reveal more details of cytoderm and make the single cell contour easy to identify, which would greatly benefit the cell morphological observation. Additionally, besides the wavelength filtered laser, even a broadband white light can be used as an illumination source to achieve switchable bright-field and phase contrast imaging (SI Figure S14). This works not only because the implemented imaging system here is coaxial and contains achromatic lenses but also due to the broadband response of the metasurface spatial filter across the entire visible frequency range.

In conclusion, we propose and demonstrate a spin-multiplexed metasurface-based optical imaging system capable of switching between bright-field and spiral phase contrast imaging modes. The metasurface spatial filter is formed by an array of subwavelength TiO_2 nanopillars and can provide two uncorrelated phase profiles corresponding to the spin states of the incident light. In the experiment, by imposing the metasurface spatial filter with a constant phase profile for LCP light and a spiral phase profile for RCP light, dynamically switchable ordinary diffraction imaging and isotropic edge-enhanced imaging are respectively demonstrated. Besides the photonic spin-controlled properties, the planar single layer and ultrathin architecture of the metasurface spatial filter realized here enables a scalable and integration friendly platform for structured light illumination, and its potential application in biomedical microscopy imaging, crystal dislocation detecting, and optical analog computing.

METHODS

Numerical Simulation. The numerical simulations shown in Figure 2 are performed using the finite-difference time-domain (FDTD) technique. The mesh grid on TiO_2 nanopillars in simulation is $g_x = g_y = g_z = 2$ nm. All the nanopillars have a fixed height of 600 nm. The phase shifts (φ_x, φ_y) are obtained by parameter sweeping of TiO_2 nanopillars' in-plane dimension D_x and D_y varying from 100 to 400 nm with a step of 5 nm. The refractive index of TiO_2 is measured using spectroscopic ellipsometry (SI Figure S3).

Sample Fabrications. Quartz substrates were first coated with hexamethyldisilazane and positive-tone electron beam resist. The resist thickness is 600 nm, which determines the height of the final TiO_2 nanopillars. Subsequently, samples were coated with 10 nm of aluminum via thermal evaporation to avoid charging effects during the electron-beam lithography step. The electron-beam lithography was done using an accelerating voltage of 125 kV and developed in hexyl acetate for 120 s. Next, the patterned samples were coated with TiO_2 using atomic layer deposition (ALD). The ALD was done at the temperature of 90 °C to ensure that the patterned resist does not deform. After this step, inductively coupled-plasma reactive ion etching (ICP-RIE) was carried out with a mixture of Cl_2 and BCl_3 gas to etch the overcoated TiO_2 until the resist layer is reached. Finally, the samples were exposed to UV irradiation, followed by soaking in *n*-methyl-2-pyrrolidone. This step removes the resist and results in TiO_2 pillar arrays with predesigned patterns.

ASSOCIATED CONTENT

Supporting Information

The Supporting Information is available free of charge at https://pubs.acs.org/doi/10.1021/acs.nanolett.0c00471.

Derivation of spiral phase masking function, spatial spectral transfer function, derivation of the Jones matrix, calculation and simulation of phase modulation in dielectric nanopillars, spectroscopic ellipsometry measured refractive index of TiO_2, effect of the segment number of spiral phase on imaging, polarization conversion efficiency of the metasurface spatial filter, investigation of the system resolution, white light illuminated bright-field, and phase contrast imaging of undyed onion epidermal cells (PDF)

AUTHOR INFORMATION

Corresponding Author

Ting Xu − *National Laboratory of Solid-State Microstructures, Jiangsu Key Laboratory of Artificial Functional Materials, College of Engineering and Applied Sciences, Nanjing University, Nanjing 210093, China; Collaborative Innovation Center of Advanced Microstructures, Nanjing 210093, China;* orcid.org/0000-0002-0704-1089; Email: xuting@nju.edu.cn

Authors

Pengcheng Huo − *National Laboratory of Solid-State Microstructures, Jiangsu Key Laboratory of Artificial Functional Materials, College of Engineering and Applied Sciences, Nanjing University, Nanjing 210093, China; Collaborative Innovation Center of Advanced Microstructures, Nanjing 210093, China*

Cheng Zhang − *School of Optical and Electronic Information and Wuhan National Laboratory for Optoelectronics, Huazhong University of Science and Technology, Wuhan 430074, China;* orcid.org/0000-0002-9739-3511

Wenqi Zhu − *Physical Measurement Laboratory, National Institute of Standards and Technology, Gaithersburg, Maryland 20899, United States; Maryland NanoCenter, University of Maryland, College Park, Maryland 20899, United States*

Mingze Liu − *National Laboratory of Solid-State Microstructures, Jiangsu Key Laboratory of Artificial Functional Materials, College of Engineering and Applied Sciences, Nanjing University, Nanjing 210093, China*

Song Zhang − *National Laboratory of Solid-State Microstructures, Jiangsu Key Laboratory of Artificial Functional Materials, College of Engineering and Applied Sciences, Nanjing University, Nanjing 210093, China*

Si Zhang − *National Laboratory of Solid-State Microstructures, Jiangsu Key Laboratory of Artificial Functional Materials, College of Engineering and Applied Sciences, Nanjing University, Nanjing 210093, China*

Lu Chen − *Physical Measurement Laboratory, National Institute of Standards and Technology, Gaithersburg, Maryland 20899, United States; Maryland NanoCenter, University of Maryland, College Park, Maryland 20899, United States*

Henri J. Lezec − *Physical Measurement Laboratory, National Institute of Standards and Technology, Gaithersburg, Maryland 20899, United States*

https://dx.doi.org/10.1021/acs.nanolett.0c00471
Nano Lett. 2020, 20, 2791−2798

Amit Agrawal − *Physical Measurement Laboratory, National Institute of Standards and Technology, Gaithersburg, Maryland 20899, United States; Maryland NanoCenter, University of Maryland, College Park, Maryland 20899, United States;* orcid.org/0000-0002-9619-7623

Yanqing Lu − *National Laboratory of Solid-State Microstructures, Jiangsu Key Laboratory of Artificial Functional Materials, College of Engineering and Applied Sciences, Nanjing University, Nanjing 210093, China; Collaborative Innovation Center of Advanced Microstructures, Nanjing 210093, China*

Complete contact information is available at: https://pubs.acs.org/10.1021/acs.nanolett.0c00471

Author Contributions

P.H., C.Z., and W.Z. contributed equally. All authors contributed to the interpretation of results and participated in manuscript preparation. T.X. directed the project.

Notes

The authors declare no competing financial interest.

■ ACKNOWLEDGMENTS

The work is supported by the National Key R&D Program of China (2016YFA0202100 and 2017YFA0303700) and National Natural Science Foundation of China (11774163). W.Z., L.C., and A.A. acknowledge support under the Cooperative Research Agreement between the University of Maryland and the National Institute of Standards and Technology, Center for Nanoscale Science and Technology, Award #70-NANB14H209, through the University of Maryland. C.Z. acknowledges the start-up funding from Huazhong University of Science and Technology.

■ REFERENCES

(1) Bradbury, S.; Evennett, P. *Contrast Techniques in Light Microscopy*; BIOS Scientific: Oxford, 1996.
(2) Goodman, J. W. *Introduction to Fourier Optics*, 3rd ed.; Roberts & Company Publishers: Englewood, CO, 2005.
(3) Zernike, F.; Stratton, F. J. M. Diffraction theory of the knife-edge test and its improved form, the phase-contrast method. *Mon. Not. R. Astron. Soc.* **1934**, *94*, 377−384.
(4) Normanski, G. Interferometry with Schlieren microscopy. *J. Phys. Radium* **1955**, *16*, 9−11.
(5) Silva, A.; Monticone, F.; Castaldi, G.; Galdi, V.; Alu, A.; Engheta, N. Performing mathematical operations with metamaterials. *Science* **2014**, *343*, 160−163.
(6) Pors, A.; Nielsen, M. G.; Bozhevolnyi, S. I. Analog computing using reflective plasmonic metasurfaces. *Nano Lett.* **2015**, *15*, 791−797.
(7) Zhu, T.; Zhou, Y.; Lou, Y.; Ye, H.; Qiu, M.; Ruan, Z.; Fan, S. Plasmonic computing of spatial differentiation. *Nat. Commun.* **2017**, *8*, 15391.
(8) Zhou, J.; Qian, H.; Chen, C.; Zhao, J.; Li, G.; Wu, Q.; Luo, H.; Wen, S.; Liu, Z. Optical edge detection based on high-efficiency dielectric metasurface. *Proc. Natl. Acad. Sci. U. S. A.* **2019**, *116*, 11137−11140.
(9) Zhu, T.; Lou, Y.; Zhou, Y.; Zhang, J.; Huang, J.; Li, Y.; Luo, H.; Wen, S.; Zhu, S.; Gong, Q.; Qiu, M.; Ruan, Z. Generalized spatial differentiation from the spin hall effect of light and its application in image processing of edge detection. *Phys. Rev. Appl.* **2019**, *11*, No. 034043.
(10) Cordaro, A.; Kwon, H.; Sounas, D.; Koenderink, A. F.; Alu, A.; Polman, A. High-index dielectric metasurfaces performing mathematical operations. *Nano Lett.* **2019**, *19*, 8418−8423.
(11) Zhou, Y.; Zheng, H. Y.; Kravchenko, I. I.; Valentine, J. Flat optics for image differentiation. *Nat. Photonics* **2020**, 1−9.
(12) Davis, J. A.; McNamara, D. E.; Cottrell, D. M.; Campos, J. Image processing with the radial Hilbert transform: theory and experiments. *Opt. Lett.* **2000**, *25*, 99−101.
(13) Swartzlander, G. A., Jr. Peering into darkness with a vortex spatial filter. *Opt. Lett.* **2001**, *26*, 497−499.
(14) Crabtree, K.; Davis, J. A.; Moreno, I. Optical processing with vortex-producing lenses. *Appl. Opt.* **2004**, *43*, 1360−1367.
(15) Furhapter, S.; Jesacher, A.; Bernet, S.; Ritsch-Marte, M. Spiral phase contrast imaging in microscopy. *Opt. Express* **2005**, *13*, 689−694.
(16) Jesacher, A.; Furhapter, S.; Bernet, S.; Ritsch-Marte, M. Spiral interferogram analysis. *J. Opt. Soc. Am. A* **2006**, *23*, 1400−1409.
(17) Jesacher, A.; Furhapter, S.; Bernet, S.; Ritsch-Marte, M. Shadow effects in spiral phase contrast microscopy. *Phys. Rev. Lett.* **2005**, *94*, 233902.
(18) Situ, G.; Pedrini, G.; Osten, W. Spiral phase filtering and orientation-selective edge detection/enhancement. *J. Opt. Soc. Am. A* **2009**, *26*, 1788−1797.
(19) Maurer, C.; Jesacher, A.; Bernet, S.; Ritsch-Marte, M. What spatial light modulators can do for optical microscopy. *Laser Photonics Rev.* **2011**, *5*, 81−101.
(20) Lin, D.; Fan, P.; Hasman, E.; Brongersma, M. L. Dielectric gradient metasurface optical elements. *Science* **2014**, *345*, 298−302.
(21) Arbabi, A.; Horie, Y.; Bagheri, M.; Faraon, A. Dielectric metasurfaces for complete control of phase and polarization with subwavelength spatial resolution and high transmission. *Nat. Nanotechnol.* **2015**, *10*, 937−943.
(22) Kruk, S.; Kivshar, Y. Functional meta-optics and nanophotonics governed by Mie resonances. *ACS Photonics* **2017**, *4*, 2638−2649.
(23) Huo, P.; Zhang, S.; Liang, Y.; Lu, Y.; Xu, T. Hyperbolic metamaterials and metasurfaces: Fundamentals and applications. *Adv. Opt. Mater.* **2019**, *7*, 1801616.
(24) Divitt, S.; Zhu, W.; Zhang, C.; Lezec, H. J.; Agrawal, A. Ultrafast optical pulse shaping using dielectric metasurfaces. *Science* **2019**, *364*, 890−894.
(25) Shaltout, A. M.; Lagoudakis, K. G.; Groep, J.; Kim, S. J.; Vuckovic, J.; Shalaev, V. M.; Brongersma, M. L. Spatiotemporal light control with frequency-gradient metasurfaces. *Science* **2019**, *365*, 374−377.
(26) Kwon, H.; Arbabi, E.; Kamali, S. M.; Fraaji-Dana, M.; Faraon, A. Single-shot quantitative phase gradient microscopy using a system of multifunctional metasurfaces. *Nat. Photonics* **2020**, *14*, 109−114.
(27) Luo, X. G. Engineering optics 2.0: a revolution in optical materials, devices, and systems. *ACS Photonics* **2018**, *5*, 4724−4738.
(28) Luo, X. G. *Engineering Optics 2.0: A Revolution in Optical Theories, Materials, Devices and Systems*; Springer Singapore: Singapore, 2019.
(29) Khorasaninejad, M.; Chen, W. T.; Devlin, R. C.; Oh, J.; Zhu, A. Y.; Capasso, F. Metalenses at visible wavelengths: Diffraction-limited focusing and subwavelength resolution imaging. *Science* **2016**, *352*, 1190−1194.
(30) Wang, S.; Wu, P. C.; Su, V.; Lai, Y.; Chen, M.; Kuo, H. Y.; Chen, B. H.; Chen, Y. H.; Huang, T.; Wang, J.; Lin, R.; Kuan, C.; Li, T.; Wang, Z.; Zhu, S.; Tsai, D. P. A broadband achromatic metalens in the visible. *Nat. Nanotechnol.* **2018**, *13*, 227−232.
(31) Zheng, G. X.; Muhlenbernd, H.; Kenney, M.; Li, G. X.; Zentgraf, T.; Zhang, S. Metasurface holograms reaching 80% efficiency. *Nat. Nanotechnol.* **2015**, *10*, 308−312.
(32) Wang, B.; Dong, F.; Li, Q. T.; Yang, D.; Sun, C.; Chen, J.; Song, Z.; Xu, L.; Chu, W.; Xiao, Y. F.; Cong, Q.; Li, Y. Visible-frequency dielectric metasurfaces for multiwavelength achromatic and highly dispersive holograms. *Nano Lett.* **2016**, *16*, 5235−5240.
(33) Guo, Y.; Pu, M.; Zhao, Z.; Wang, Y.; Jin, J.; Gao, P.; Li, X.; Ma, X.; Luo, X. Merging geometric phase and plasmon retardation phase in continuously shaped metasurfaces for arbitrary orbital angular momentum generation. *ACS Photonics* **2016**, *3*, 2022−2029.
(34) Zhang, F.; Pu, M.; Luo, J.; Yu, H.; Luo, X. Symmetry breaking of photonic spin-orbit interactions in metasurfaces. *Opto-Electronic Engineering* **2017**, *44*, 319−325.

(35) Zhang, F.; Pu, M.; Li, X.; Gao, P.; Ma, X.; Luo, J.; Yu, H.; Luo, X. All-dielectric metasurfaces for simultaneous giant circular asymmetric transmission and wavefront shaping based on asymmetric photonic spin-orbital interactions. *Adv. Funct. Mater.* **2017**, *27*, 1704295.
(36) Ling, X. H.; Zhou, X. X.; Huang, K.; Liu, Y. C.; Qiu, C. W.; Luo, H. L.; Wen, S. C. Recent advances in the spin Hall effect of light. *Rep. Prog. Phys.* **2017**, *80*, No. 066401.
(37) Pu, M. B.; Li, X.; Ma, X. L.; Wang, Y. Q.; Zhao, Z. Y.; Wang, C. T.; Hu, C. G.; Gao, P.; Huang, C.; Ren, H. R.; Li, X. P.; Qin, F.; Yang, J.; Gu, M.; Hong, M. H.; Luo, X. G. Catenary optics for achromatic generation of perfect optical angular momentum. *Science Advances* **2015**, *1*, No. e1500396.
(38) Huo, P.; Zhang, S.; Fan, Q.; Lu, Y.; Xu, T. Photonics spin-controlled generation and transformation of 3D optical polarization topologies enabled by all-dielectric metasurfaces. *Nanoscale* **2019**, *11*, 10646−10654.
(39) Bao, Y. J.; Ni, J. C.; Qiu, C. W. A minimalist single-layer metasurface for arbitrary and full control of vector vortex beams. *Adv. Mater.* **2020**, *32*, 1905659.
(40) Tittl, A.; Leitis, A.; Liu, M.; Yesilkoy, F.; Choi, D. Y.; Neshev, D. N.; Kivshar, Y. S.; Altug, H. Imaging-based molecular barcoding with pixelated dielectric metasurfaces. *Science* **2018**, *360*, 1105−1109.
(41) Koshelev, K.; Tang, Y. T.; Li, K. F.; Choi, D. Y.; Li, G. X.; Kivshar, Y. Nonlinear metasurfaces governed by bound states in the continuum. *ACS Photonics* **2019**, *6*, 1639−1644.
(42) Hu, G.; Hong, X.; Wang, K.; Wu, J.; Xu, H. X.; Zhao, W.; Liu, W.; Zhang, S.; Garcia-Vidal, F.; Wang, B.; Lu, P.; Qiu, C. W. Coherent steering of nonlinear chiral valley photonics with a synthetic Au-WS_2 metasurface. *Nat. Photonics* **2019**, *13*, 467−472.
(43) Khorasaninejad, M.; Chen, W. T.; Zhu, A. Y.; Oh, J.; Devlin, R. C.; Rousso, D.; Capasso, F. Multispectral chiral imaging with a metalens. *Nano Lett.* **2016**, *16*, 4595−4600.

https://dx.doi.org/10.1021/acs.nanolett.0c00471
Nano Lett. 2020, 20, 2791−2798